RESEARCH ARTICLE

Macromolecular Materials and Engineering
www.mame-journal.de

# Melt Electrowriting of Poly(dioxanone) Filament Using a Multi-Axis Robot

*Simon Luposchainsky, Sven Jörissen, Andreas Nüchter,* and Paul D. Dalton**

**Excessive thermal degradation is one limitation of scaffold production by melt electrowriting (MEW). This is particularly pertinent when using higher melting point polymers with faster degradation profiles in vivo for tissue engineering applications. This is addressed here by switching from a pneumatic to a filament-based feeding system and demonstrating the processing of a medical polymer, poly(dioxanone) (PDO). Additionally, by replacing the established cartesian printer configuration with a six-axis robotic arm, arbitrary nonplanar surfaces can be used as a fiber collector, as shown here by using a spherical collector. The combination of these techniques allows MEW to be used more broadly in tissue engineering where currently established medical polymers are incompatible with the process, or the geometric shapes of scaffold are to be expanded. It demonstrates the required technology to produce nonplanar scaffolds of PDO in a dome shape with dimensions for a biodegradable corneal implant.**

## 1. Introduction

One challenge in tissue engineering and regenerative medicine (TERM) is the creation of scaffolds that mimic the properties of the tissue they are intended to replace.[1,2] Scaffolds provide multiple functions; they must promote cell growth and attachment, allow nutrient perfusion, and have sufficient initial mechanical strength. The scaffold should also slowly disappear from the tissue at the appropriate rate while being replaced with neo-tissue.[3] It is for this reason that hydrolytically-degradable polyesters are an attractive class of clinical biomaterials. Polyesters with a history of clinical use include poly($\epsilon$-caprolactone) (PCL), poly(glycolide), poly(lactide), and poly(dioxanone) (PDO);[4] they all have different hydrolytic degradation rates based on their chemistries.[5] PDO, for example, is a 6-month biodegradable polymer that is used as a suture in the clinic.[4,6]

In Additive Manufacturing (AM), parts and features are created by fusing material only where required to achieve the desired geometry of the object that is to be produced.[7] There are many different AM technologies developed for TERM scaffolds[8,9] including those with increasing resolutions and complexity.[10,11] For additively manufactured TERM scaffolds, melt extrusion of thermoplastic polyesters is particularly attractive,[12] and is processed from pellet or filament form without the use of additives or fillers to enhance processability.[13] As exemplified by additively manufactured PCL scaffolds for non-load-bearing bones,[14] melt processing is a successful path to the clinic.

Electrohydrodynamic (EHD) processing of polymer melts navigates both the regulatory and material constraints required for clinical translation while producing smaller feature sizes.[12] Examples of EHD processing include melt electrospinning (MES) and melt electrowriting (MEW), which produce fibers down to 270 or 350 nm, respectively.[15,16] To achieve these sub-micron diameters for MES/MEW, however, a reduction in the mass flow rate is required that results in extended heating times. PCL is a standout polyester in that it thermally degrades almost negligibly when kept just above its melting temperature of 60 °C.[17]

Therefore, PCL has become the gold standard polymer used for MEW, during its initial development. The majority of MEW scaffolds are also made on flat collectors. A mandrel collector is used for MEW tubes, while several reported placing an object (i.e., a dome, ramp) onto an X-Y collector.[18,19] Achieving a higher degree of freedom through a multi-axis robot is necessary, however, to accurately direct-write onto a steeply curved surface using MEW.[18] Electrical fields will affect the deposition of fibers and in this study, a multi-axis robot was used to maintain this constant electric field onto a dome collector. This allows the deposition of fibers while maintaining perpendicularity of the printhead to the collector surface at a set distance.

PCL has a long hydrolytic degradation of 2–3 years.[13,20] Such periods are sometimes not desired in TERM, and more readily

S. Luposchainsky, P. D. Dalton
Phil and Penny Knight Campus for Accelerating Scientific Impact
University of Oregon
1505 Franklin Boulevard, Eugene, OR 97403, USA
E-mail: pdalton@uoregon.edu
S. Luposchainsky, P. D. Dalton
Department for Functional Materials in Medicine and Dentistry
University Würzburg
Pleicherwall 2, 97070 Würzburg, Germany
S. Jörissen, A. Nüchter
Informatics VII – Robotics and Telematics
Julius-Maximilians-University Würzburg
Am Hubland, 97074 Würzburg, Germany
E-mail: andreas@nuechti.de

The ORCID identification number(s) for the author(s) of this article can be found under https://doi.org/10.1002/mame.202200450



**DOI: 10.1002/mame.202200450**

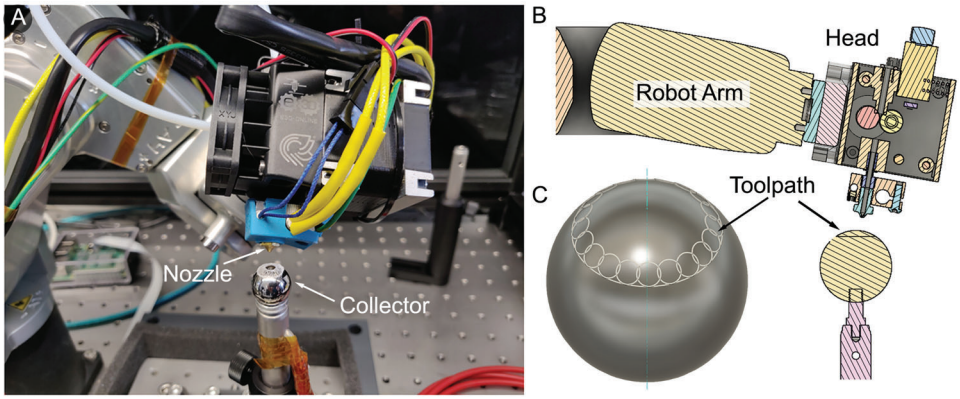


**Figure 1.** A) Closeup of the MEW print head in position, with the collector, collector mount, and cable all visible. B) Cross-section view of the center plane of the robot and MEW head with filament path and feed system and hot end consisting of heat break, aluminum block, and nozzle all shown. A 30 mm spherical collector is shown for scale. C) Schematic view of a sample toolpath as generated by Python script.

degradable materials are used.[21,22] This, in turn often results in faster thermal degradation, which poses a challenge for MEW, due to the low flow rates required and the common "syringe reservoir" approach for the melt. Therefore, a filament-based approach with reduced heating time is developed and shown here. We demonstrate proof in principle MEW processing of PDO filament, and mount this on a multi-axis robot to direct write upon a sphere.

## 2. Experimental Section

### 2.1. Materials

Medical grade Dioxaprene 100 M 1.75 mm filament (Lot #48 678; Poly-Med Inc., United States) was gratefully received as a gift and used as received with properties shown in Table S1 (Supporting Information). To convert the measured PDO mass into volume, a density of 1.318 g $cm^{-3}$ was used. It is also highly recommended to use filament as soon as acquired, as noticeable handling differences are observable after a year of room temperature storage (Figure S1, Supporting Information).

### 2.2. MEW Robot Printer and Process Parameters

The MEW robot printer was mounted onto a B6090L optical breadboard (Thorlabs GmbH, Germany). An aluminum frame holding acrylic sheets with a frontal side-opening door was designed for a controlled and reduced dust environment, safety, and protection. The enclosure covers the majority of the base plate area of the machine, leaving gaps to feed through cables. **Figure 1**A shows the completed setup while all described components are shown in Figure S2 (Supporting Information).

A collector distance of 4 mm was selected and maintained throughout. The filaments were cut into short segments of ≈350 mm length to fit into the head-mounted Teflon magazine for all experiments. All experiments were performed at 20–45% relative humidity and at an ambient temperature of 18–21°C. Further information regarding the robot MEW printer is provided in the Supporting Information.

### 2.3. MEW Print Head Design

The MEW print head was based on the E3D Hemera 1.75 (E3D-Online Ltd.), which comes as a complete set of parts and connection cables to assemble a working print head. It is also modular, and all sensors and hot end components can be exchanged/replaced. The filament was fed through the MEW head nozzle at defined speeds to heat it to a molten, printable state. Advancing the filament toward the nozzle typically involves pushing it through a narrow channel by a toothed pulley that is driven by a stepper motor through a set of gears. The nozzle and heater are near this feeding mechanism to minimize filament buckling and breakage.

Heating is achieved at a "hot zone" within the nozzle metal block that was thermally isolated from the feeding mechanism and electrically heated. At 400 g, the MEW head weighs less than the 500 g payload limit of the Meca500 robot arm. The print head uses a gear reduction of 3.32:1 and has a minimized distance between the feeding gears and the hot zone. The hot end design with an aluminum heater block, brass nozzle, and 30 W heating cartridge is a de facto standard for most open-source desktop Fused Deposition Modeling (FDM) 3D printers.

During assembly, a copper ground wire was connected to the heater block with a set screw that also held the heater cartridge in position to provide a safe path for electrical discharge in case of arcing. The heat break that connects the heater block to the motor body was coated with boron nitride paste (Slice Engineering, United States) prior to installation for a sharper thermal transition from filament to melt.

The print head was mounted to the Meca500 with a 3D printed base plate that has multiple functions. It connects the print head to the robot tool flange plate at a defined position while being as lightweight and stiff as possible, and it electrically isolates the robot from the print head. The 0.4 mm print nozzle orifice or tool center point (TCP) is thus fixed 30 mm away from and 40 mm offset below the robot flange. A schematic cross-section of the mounted print head setup can be seen in Figure 1B. A 350 mm segment of 4 mm outer and 2 mm inner diameter Teflon tubing was connected to the input coupling of the print head, sealed on the other end with a screw, and connected to

the base plate, forming a sealed arc that serves as a reservoir of filament for printing without air exposure.

### 2.4. Print Head Control Hardware and Setup

To control the print head stepper motor and temperature, a Duet 2 Ethernet (Duet3D limited, United Kingdom) was used. It offers connectivity for up to five stepper motors, three heaters and temperature sensors, cooling fans and further expandability. It was powered with an RSP-320-24 24 V switching power supply (MEAN WELL Enterprises Co. Ltd., Taiwan).

### 2.5. Collector Configuration

The high voltage was applied to the spherical collector and generated with an LNC-10000-2-neg power supply (Heinzinger electronic GmbH, Germany). The collector area consists of a MB1015S/M breadboard (Thorlabs GmbH, Germany) that is mounted on a custom 30 mm thick Delrin base plate for electrical isolation. To position the collector freely in the robot workspace, optical posts (UPH100/M and TR100/M, Thorlabs GmbH, Germany) were used, providing a magnetic connection to the breadboard that prevents damaging any components in case of a collision.

All scaffolds shown were produced with a 15 mm diameter spherical collector and a programmed toolpath perpendicular to the collector surface. To better analyze print quality, a removable collector consisting of a 15 mm diameter ball bearing fixed to an aluminum stub with conducting carbon cement (Agar Scientific, United Kingdom) that slots into the M4 thread of the optical post was used and can be seen in place after a print in Figure 1A.

After a purge of the filament prior to the start of printing at each flow rate, scaffolds were produced every 20 min for a total experiment duration approximately of 160 min to investigate thermal degradation of the polymer. This was performed for the extrusion speeds F60, F90, and F120, which correspond to volumetric flow rates of 21.6, 32.5, and 43.3 $\mu L\ h^{-1}$, respectively, and it was foundedthat 32.5 $\mu L\ h^{-1}$ proved to be the most stable and thus suitable for the given robot toolpath and speeds.

### 2.6. Camera and Monitoring

For print monitoring and calibrating the collector position, a Raspberry Pi 4B was set up with a Raspberry HQ camera sensor and 16 mm Telephoto lens (Raspberry Pi Foundation, United Kingdom). Images and videos recorded the molten material exiting the nozzle and were used to observe jet formation. The Raspberry Pi was powered with a USB power supply and connected to the controlling computer via ethernet connection.

### 2.7. Software

Fusion 360 CAD/CAM software package (Autodesk Inc, United States) was used to design enclosures and adapters. The 3D model was later partially exported as an STL file to allow for accurate simulation of the Robot in the RoboDK suite. The 3D model was also used to generate toolpaths for preliminary testing of jet formation during printing with its multi-axis CAM functionality.

RoboDK (RoboDK Inc., Canada) version 5.1.1.19121 was chosen for offline robot programming and to directly control and program the robot. It offers a modular, Python-based design and provides a post-processor specific for the Meca500, allowing the robot to be controlled from a PC via its application programming interface. RoboDK was used to position the robot, calibrate the collector position, and plan and simulate toolpaths for the printing of scaffolds. Video S1 (Supporting Information) shows a simulated sample toolpath and printer operating simultaneously.

A 3D model of the relevant components was imported and used to help visualize potential problems or out-of-reach positions for the simulation and program generation process. This application does not need the rotational symmetry of the print head nozzle and it was decided to not consider the rotational position of the TCP along the filament axis of the tool head for planning the robot paths used for printing. Singularities are where joints in the arm need to be repositioned to continue toolpath motion and are shown in Video S2 (Supporting Information). As discussed later, these deleteriously affect constant tool head velocity.

### 2.8. Printing Toolpath

Python programming was used to generate the G-code input required to generate the robot toolpath. The program generates a point cloud of successive coordinates with normal vectors that represent the positions of the TCP the robot must follow to generate a scaffold. The geometry formed by the point cloud is that of a ring of circles approximately normal to the center of the collector sphere and connected by a larger circle as can be seen in a schematic view in Figure 1C. The points were generated in G-code readable form and based on five input values: Sphere radius, print distance, the lower bound of the toolpath with respect to the center of the sphere, the radius of circles generated, and the number of circles generated. The Python script is made available in the Supporting Information.

The overlapping circular toolpath (Figure 1C) used in this approach results in multiple fiber junctions to ensure scaffold stability as well as an accumulation of material around the rim to reinforce suture anchoring. The circle-based path also allows direct visual monitoring of printing performance, particularly whether the desired constant translation speed is maintained.

### 2.9. Measurement Equipment

Sample imaging and fiber count were visualized with a Zeiss discovery V20 Stereomicroscope (Carl Zeiss AG, Germany). The morphological analysis of select samples was performed using scanning electron microscopy (SEM). Samples were transferred as produced and attached to the collector into a Leica EM ACE600 sputter coater (Leica Camera AG, Germany) and coated with 3.5 nm Platinum for sufficient electron dispersion. Imaging was then performed with a crossbeam 340 SEM with a Zeiss Gemini e-Beam column (Carl Zeiss AG, Germany). The samples were weighed on an XPE26 DeltaRange scale (Mettler, Toledo, USA).

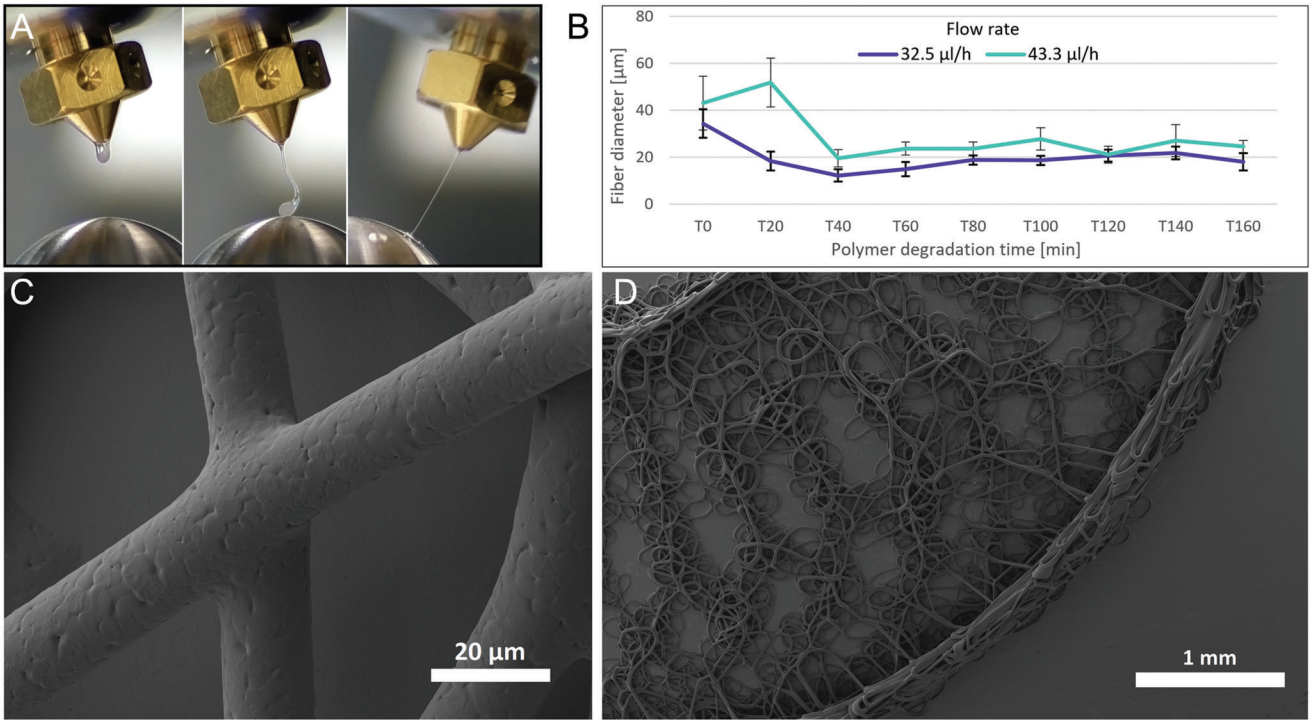


**Figure 2.** A) PDO jet creation and MEW. The time between left and center image is 15 s, right image shows the print head in motion displaying the jetting behavior of the polymer with deposition in nonlinear pattern due to insufficient print head speed. B) Fiber diameters for scaffolds printed at flows 32.5 and 43.3 µL $h^{-1}$ show a decreasing fiber diameter over time, with an expected plateauing of fiber diameter once a steady state of melt degradation over time is reached. Marked time points denote start times of individual scaffold printing. C) Fiber-fiber junction with visible fusion after 2 h of continuous extrusion at 32.5 µL $h^{-1}$. D) Wider view of scaffold produced at 32.5 µL $h^{-1}$ after 2 h of printing.

The thermal properties of the filament were observed using a DSC 204 F1 Phoenix (Netzsch-Gerätebau GmbH, Germany). Samples with a mass of ≈5 mg were placed in an aluminum crucible with a pierced lid and heated to 200 °C at 10 K $min^{-1}$ and held at 200 °C for 10 min before cooling to −50 °C at a rate of 10 °C $min^{-1}$ for three heating and two cooling cycles (Figure S3, Supporting Information). DSC outcomes are listed in Table S2 (Supporting Information) and are in line with previous DSC research on PDO.[23]

## 3. Results and Discussion

The 4 mm collector distance used in this study is similar to distances used in other MEW configurations[17] and offered an acceptable tolerance zone at the chosen high voltage to prevent arcing for the chosen calibration procedure of print head and collector. Similarly, we could readily observe the Taylor cone and jet formation, as well as remove the samples off the collector. Video S3 (Supporting Information) shows a close up of the jet initiation and fiber deposition. Figure S1 (Supporting Information) shows how PDO filament that is stored longer was brittle and "waxy" compared to fresh filament that was ductile. This change in mechanical properties correlates with observed changes in the DSC, where the size of the crystallization peak after storage is reduced. The baseline spectrum acquired here is in line with those previously reported for PDO.[23]

### 3.1. Printing Outcomes

The first generation of a MEW jet for PDO was successfully achieved at a set temperature of 120 °C. However, to consistently extrude a homogenous melt, the print temperature for scaffold production was set at 135 °C. As can be seen in **Figure 2**A, the starting material droplet is quickly solidified and the jet only anchors onto the collector after movement.

### 3.2. Achieving the Critical Translation Speed

Using this compiled code with the described setup for MEW printing of PDO, scaffolds could be produced successfully using flow rates from 32.5 to 54.1 µL $h^{-1}$. However, two key observations were made at this stage:

First, the robot's speed along the toolpath is unfortunately not as constant as desired, particularly at the lower and upper bounds of the circles where the nozzle has to be reoriented to move from one small circle to the next while still aiming at the collector. This has the desirable effect of depositing more material at the border of the produced constructs for enhanced mechanical strength, but greatly impacts the jet deposition and stability for the same reason, as the speed and thus forces the jet experiences are not constant for the duration of scaffold production. For this reason, the robot speed of 600 mm $min^{-1}$ was selected previously, as it was found to strike a suitable

**Table 1.** Comparison of calculated and measured weight of produced scaffolds at programmed volumetric flow rates.

| Programmed flow rate [μL /h$^{-1}$] | Expected mass [mg] | Measured mass [mg] |
|---|---|---|
| 32.5 | 3.57 | 3.77 ± 0.23 |
| 43.3 | 4.76 | 5.00 ± 0.26 |

balance with the chosen MEW parameters that could maintain a jet well at the tested flow rates in most cases.

Second, the MEW jet speed and deposited scaffold morphology varied greatly depending on the breaks between experiments and the varying age of the melt. One example can be seen in Figure 2, where a scaffold printed at a flow rate of 32.5 μL h$^{-1}$ is shown through SEM imaging to observe fiber morphology.

With a different robotic setup or target geometry that allows for printing at higher speeds, straight fibers should be attainable as the limiting parameter is the maximum constant robot speed along a spherical toolpath in this study.

### 3.3. Thermal Degradation of the Polymer

The scaffold mass for each flow rate is presented in **Table 1**. MEW processing at 21.6 μL h$^{-1}$ was unstable and poor outcome prints are shown in Figure S4 (Supporting Information). For flow rates of 32.5 μL h$^{-1}$, all scaffolds could be printed successfully, and only the scaffold at 40 min displayed minor instabilities that could be observed during the printing process. For 43.3 μL h$^{-1}$ of flow, all scaffolds could be printed successfully, with instabilities occurring for scaffolds at 40 and 100 min. The measured fiber diameters can be seen in Figure 2B, with establishment of a steady state diameter after over an hour of printing.

At these flow rates, the melt within the print head is replaced by freshly melted filament in its entirety after ≈67 min for 32.5 μL h$^{-1}$ and 50 min for 43.3 μL h$^{-1}$. This is in agreement with the measured fiber diameter change over time, as it remains relatively constant once a steady state of degradation in the advancing melt is reached. Given a 5 min print time for all scaffolds, we calculate the expected mass of the produced scaffolds as previously described, the results of that are summarized in Table 1. The calculated mass is in good agreement with the experimentally derived values.

Ordered fiber stacking could be observed to varying degrees, with lower degradation times and higher flow rates (43.3 μL h$^{-1}$) producing more ordered scaffolds (Figure S5, Supporting Information). Since the higher flow rate leads to higher fiber diameters and a lower degradation implies a higher melt viscosity, this is in agreement with established MEW principles,[24] as such conditions lower the CTS of the process and allow the robot to deposit more stacked fibers at the speeds it is programmed to run.

All produced scaffolds had an outer diameter of 10 mm and an inner diameter of 3.5 mm, a height of 2 mm, and an outer rim height of 0.5–0.8 mm due to the overlapping of the printed fibers

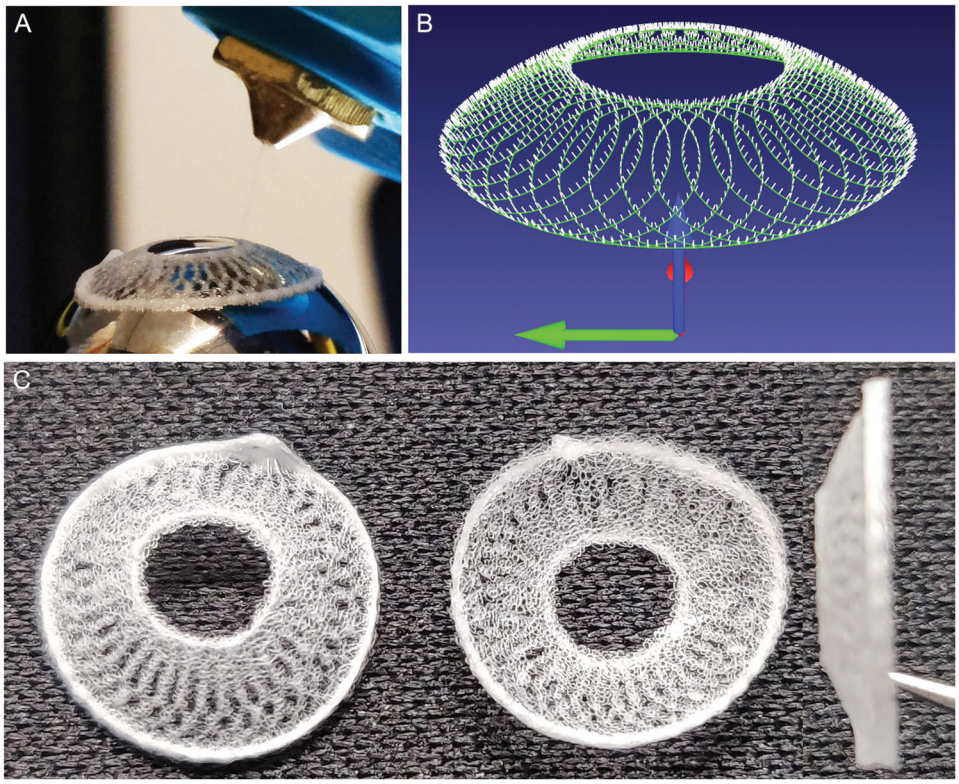


**Figure 3.** Overview of scaffolds after an equilibrium of degradation and extrusion is reached at a flow rate of 32.5 μL h$^{-1}$. A) print in progress, B) the programmed path resulting in the morphology shown below. C) Front, back, and side of scaffold view at the macro scale. Scaffold outer diameter 10 mm for all images.

at the top and bottom rim of the scaffold. Each scaffold had a print time of 5 min with a pause between each print spaced 15 min apart. With increasing degradation times, the lowered viscosity caused thinner fibers and faster jets, resulting in less controllable fiber deposition. While it was not possible to continuously print above CTS with the given collector geometry and toolpath, the deposition of fibers was localized and still created the intended scaffold geometries. The outer rim of scaffolds caused significant material accumulation and stiffness of these sections, which was also observed to a lesser extent for the center ring. These characteristics are beneficial for the envisioned use case, as it provides a high surface area of thinner fibers for cells and matrix attachment in the area of the scaffold, while providing high strength for structural integrity and suture attachment at the outer rim.

The most promising scaffolds are shown in **Figure 3**, where a steady manufacturing state produced up to 10 consistent scaffolds per hour with a flow rate of 32.5 µL $h^{-1}$. Future perspectives include studies on the mechanical properties, cell interactions, and further processing steps required for a functional prosthesis before scale-up of scaffold production has to be considered. A collector sphere diameter of 15 mm was selected to create scaffolds with curvature similar to the rabbit's eye, a common pre-clinical model for the artificial cornea.[25]

## 4. Conclusion

This study provides insight into several previously unexplored aspects of MEW. These include the processing of PDO, the use of a filament feeding system, and the use of a multi-axis robot for producing dome structures. Due to the printer configuration and joint movement associated with the use of a multi-axis robot and the limitations imposed through resulting singularities, all the prints were performed below the CTS. Further improvements to this proof-of-principle study should improve the deposition accuracy and diameter control of the PDO fiber. The influence of in-process thermal degradation on the mechanical and degradation characteristics of scaffolds can also be systematically investigated with this filament-based approach. The ability to process both filament and PDO expands the types of biomedical devices that can be made using MEW.

## Supporting Information

Supporting Information is available from the Wiley Online Library or from the author.

## Acknowledgements

This work was supported by the Vogel Stiftung Dr. Eckernkamp. The technical assistance of Mr. Harald Hümpfer and Mr. Anton Hofmann is greatly appreciated. The authors would also like to thank Mr. Philipp Stahlhut for his support with SEM imaging.

Open Access funding enabled and organized by Projekt DEAL.

## Conflict of Interest

The authors declare no conflict of interest.

## Data Availability Statement

The data that support the findings of this study are available from the corresponding author upon reasonable request.

## Keywords

3D printing, electrohydrodynamics, melt electrospinning writing, robot control

Received: August 29, 2022
Revised: September 6, 2022
Published online:

[1] D. W. Hutmacher, T. Schantz, I. Zein, K. W. Ng, S. H. Teoh, K. C. Tan, *J. Biomed. Mater. Res.* **2001**, *55*, 203.
[2] R. Langer, J. P. Vacanti, *Tissue Eng. Science* **1993**, *260*, 920.
[3] D. W. Hutmacher, *Biomaterials* **2000**, *21*, 2529.
[4] D. W. Hutmacher, J. C. H. Goh, S. H. Teoh, *Ann. Acad. Med. Singap.* **2001**, *30*, 183.
[5] M. Bartnikowski, T. R. Dargaville, S. Ivanovski, D. W. Hutmacher, *Prog. Polym. Sci.* **2019**, *96*, 1.
[6] C. P. Ooi, R. E. Cameron, *J. Biomed. Mater. Res.* **2002**, *63*, 280.
[7] I. Campbell, D. Bourell, I. Gibson, *Rapid Prototyp. J.* **2012**, *18*, 255.
[8] A. Fernández-Colino, S. Jockenhoevel, in *Textile-Reinforced Scaffolds for Vascular Tissue Engineering*, (Eds: B. H. Walpoth, H. Bergmeister, G. L. Bowlin, D. Kong, J. I. Rotmans, P. Zilla), Tissue-Engineered Vascular Grafts, Springer International Publishing, Cham, **2020**, pp. 339-363.
[9] P. A. Wieringa, A. R. Gonçalves De Pinho, S. Micera, R. J. A. Wezel, L. Moroni, *Adv. Healthcare Mater.* **2018**, *7*, 1701164.
[10] G. Weisgrab, O. Guillaume, Z. Guo, P. Heimel, P. Slezak, A. Poot, D. Grijpma, A. Ovsianikov, *Biofabrication* **2020**, *12*, 045036.
[11] C. Vaquette, W. Fan, Y. Xiao, S. Hamlet, D. W. Hutmacher, S. Ivanovski, *Biomaterials* **2012**, *33*, 5560.
[12] A. Youssef, S. J. Hollister, P. D. Dalton, *Biofabrication* **2017**, *9*, 012002.
[13] M. A. Woodruff, D. W. Hutmacher, *Prog. Polym. Sci.* **2010**, *35*, 1217.
[14] F. A. Probst, D. W. Hutmacher, D. F. Müller, H.-G. Machens, J.-T. Schantz, *Handchir. Mikrochir. Plastische Chir.* **2010**, *42*, 369.
[15] K. F. Eichholz, I. Gonçalves, X. Barceló, A. S. Federici, D. A. Hoey, D. J. Kelly, *Addit. Manuf.* **2022**, *58*, 102998.
[16] C. Großhaus, E. Bakirci, M. Berthel, A. Hrynevich, J. C. Kade, G. Hochleitner, J. Groll, P. D. Dalton, *Small* **2020**, *16*, 2003471.
[17] C. Böhm, P. Stahlhut, J. Weichhold, A. Hrynevich, J. Teßmar, P. D. Dalton, *Small* **2022**, *18*, 2104193.
[18] C. D. O'Connell, O. Bridges, C. Everett, N. Antill-O'Brien, C. Onofrillo, C. Di Bella, *Adv. Mater. Technol.* **2021**, *6*, 2100345.
[19] U. Saha, R. Nairn, O. Keenan, M. G. Monaghan, *Macromol. Mater. Eng.* **2021**, *306*, 2100496.
[20] H. Sun, L. Mei, C. Song, X. Cui, P. Wang, *Biomaterials* **2006**, *27*, 1735.
[21] P. Gentile, V. Chiono, I. Carmagnola, P. Hatton, *Int. J. Mol. Sci.* **2014**, *15*, 3640.
[22] R. Langer, *Acc. Chem. Res.* **2000**, *33*, 94.
[23] M. A. Sabino, J. L. Feijoo, A. J. Müller, *Macromol. Chem. Phys.* **2000**, *201*, 2687.
[24] A. Hrynevich, B. Ş. Elçi, J. N. Haigh, R. Mcmaster, A. Youssef, C. Blum, T. Blunk, G. Hochleitner, J. Groll, P. D. Dalton, *Small* **2018**, *14*, 1800232.
[25] G. J. Crawford, T. V. Chirila, S. Vijayasekaran, P. D. Dalton, I. J. Constable, *J. Refractive Surg.* **1996**, *12*, 525.